Electron Vortex Production and Control Using Aberration Induced Diffraction Catastrophes

T. C. Petersen,[1,3,*] M. Weyland,[2,3] D. M. Paganin,[1] T. P. Simula,[1] S. A. Eastwood,[1] and M. J. Morgan[1]

[1]*School of Physics, Monash University, Victoria 3800, Australia*

[2]*Department of Materials Engineering, Monash University, Victoria 3800, Australia*

[3]*Monash Centre for Electron Microscopy, Monash University, Victoria 3800, Australia*

(Received 21 August 2012; published 14 January 2013)

An aberration corrected electron microscope is used to create electron diffraction catastrophes, containing arrays of intensity zeros threading vortex cores. Vortices are ascribed to these arrays using catastrophe theory, scalar diffraction integrals, and experimentally retrieved phase maps. From measured wave function phases, obtained using focal-series phase retrieval, the orbital angular momentum density is mapped for highly astigmatic electron probes. We observe vortex rings and topological reconnections of nodal lines by tracking the vortex cores using the retrieved phases.

DOI: 10.1103/PhysRevLett.110.033901 PACS numbers: 42.30.Rx, 05.45.−a, 41.85.−p, 68.37.Og

Quantized vortices in propagating electron waves are of interest for electron wave- function phase mapping, since in-line holography approaches can fail in the presence of these wave front dislocations [1]. In this context, electron vortices were theoretically shown to arise from the transmission of fast electrons through an atomic lattice [2]. Recent experiments have shown how electron vortices may be produced and controlled. For example, cleaved steps of graphite films can act as approximate spiral phase masks, giving rise to dislocations in electron biprism interference fringes, thereby producing vortices [3]. It has been suggested that these screw-type phase singularities may be ubiquitous for specimens with heterogeneous thickness variations on the nanoscale [3]. However, our simulations of carbon phase objects with such thickness variations suggest that specimen geometry is important and that electron vortices are not readily produced. The coherent superposition of distorted plane waves is expected to give rise to vortices. By analogy with three-wave interference in light optics [4], we expect to experimentally observe electron vortices for Bragg diffraction from crystalline specimens. Indeed, in biprism interference patterns from crystalline specimens, one can find examples of forked dislocations [5], which are signatures of quantized phase vortices. Similarly, the hallmarks of three-wave electron interference (which is a classical method for vortex production [6]) are evident for three-beam electron diffraction from crystals [7–10]. Recently, controlled vortex beams were demonstrated using micron-scale forked masks in a transmission electron microscope (TEM) [11,12].

Electron vortex beams open up new avenues for revealing specimen properties on the nanoscale. For example, Verbeeck *et al.* [11] exploited the orbital angular momentum (OAM) in a vortex beam to create a dichroic effect for $2p_{1/2} \rightarrow 3d$ and $2p_{3/2} \rightarrow 3d$ inelastic transitions in Fe. Related experiments for subnanometer spatial resolution have since been explored using spiral masks [13] and forked masks placed in the illumination aperture of the TEM [14]. It seems plausible to associate electron beams that contain vortices with probes that can promote the exchange of OAM. However, Berry [15] has cautioned against a direct association, demonstrating that OAM is not precisely connected with the presence of vortices in general. Nevertheless, the OAM density can vary significantly across an electron beam containing vortices. For light optics, astigmatism aberrations can impart significant OAM onto Gaussian beams [16].

Quantized phase vortices have also been studied intensively in visible light optics [17–19], x-ray optics [20], for microwaves [21], and acoustics [22]. For optical wave fields it is known that diffraction catastrophes [23] give rise to caustics. Diffraction catastrophes are generic to optical wave fields and are stable with respect to perturbations; i.e. they persist upon continuously varying aberrations, such as free space propagation, maintaining recognizable shapes such as linear ''folds'' or pointed ''cusps'' [23,24]. Diffraction catastrophes and phase discontinuities generally form in the focal volumes of lenses with aberrations [25,26]. Berry *et al.* [17] demonstrated the elliptic umbilic catastrophe using a triangular lens formed by water. Further, it was shown that the associated diffraction detail can be accurately approximated using superposition of plane waves, which create a lattice of phase vortices. The generation of vortex lattices by the superposition of three plane waves [4,6], or distorted spherical waves [27], has been studied in wave optics and, more recently, in Bose-Einstein condensates [28,29]. The analysis of umbilic and cusp catastrophes by Berry *et al.* [17] demonstrates that vortical wave fields can be formed by lenses with aberrations.

Optical caustics formed by primary aberrations have been widely recognized since the pioneering work of Nijboer and Nienhuis [30–32]. Caustics arising from lens aberrations in the TEM have also been characterized theoretically using geometric optics [33]. Primary aberrations can induce diffraction catastrophes; in particular, the umbilic foci for astigmatism and coma have been shown to be hyperbolic

[34]. Caustics are routinely observed when TEM illumination apertures are removed to include electron trajectories deflected through large angles. These rays do not produce significant interference effects in the probe intensity, since the removal of probe-forming apertures degrades the spatial coherence, which would seem to exclude the possibility of observing phase dislocations arising from diffraction catastrophes. However, partial coherence can be improved if small illumination apertures are used. Diffraction catastrophes can then be explored by imposing significant probe forming aberrations to disturb the point focus and create severely distorted coherent electron probes.

We have conducted experiments to produce and manipulate electron vortices in the specimen plane of a TEM, employing lens aberrations to create diffraction catastrophes. We used a Titan^3 80–300 TEM (FEI) that provides dual aberration correction (CEOS GmbH) of both the illumination and imaging lenses. Operating at an acceleration voltage of 300 kV, imaging lens aberrations were corrected to third order and the microscope was set up in the bright field imaging mode to minimize the semiangle subtended by the field emission gun source. A 10 μm condenser aperture was selected; the resulting intensity distribution was a small yet parallel probe. By adjusting the condenser lenses, the illumination was focused in the specimen plane to produce a far-field diffraction pattern of the circular condenser aperture in the form of Airy rings. The circular symmetry of these rings was then broken by increasing twofold condenser astigmatism, producing a sharp (subnanometer) line focus streaking along one direction. Through-focus propagation of the resulting distorted electron probe, using the imaging lens, revealed the presence of four umbilic foci, which outlined the caustic of the probe. The electron probe cross section and decorating diffraction detail maintained form as the probe was imaged throughout the focal series. This observed persistence of form and stability under perturbations is a key aspect of a diffraction catastrophe.

Figure 1(a) shows the logarithm of an astigmatic experimental electron probe imaged near one of the line foci. Figure 1(b) shows the same probe imaged several hundred nanometers further along the optic axis. Since the electron optical configuration was chosen to optimize the spatial coherence, the diffraction pattern was quite dim. Accordingly, the acquisition times were 100 s per probe pattern. Comparing Figs. 1(a) and 1(b), the stability of the umbilic features with respect to smooth variation of the electron wave (changing focus) implies the formation of a diffraction catastrophe. Electron trajectories make very small angles with the optic axis and we can assume paraxial imaging conditions. If we further ignore chromatic aberrations or the spread of energies in the electron source, we can utilize the diffraction theory of aberrations based upon the Huygens-Fresnel principle [35]. To this end, we consider the condenser lens aberrations as modifying the optical path lengths of spherical waves originating from a circular aperture $A(x, y)$. Fresnel propagation from the

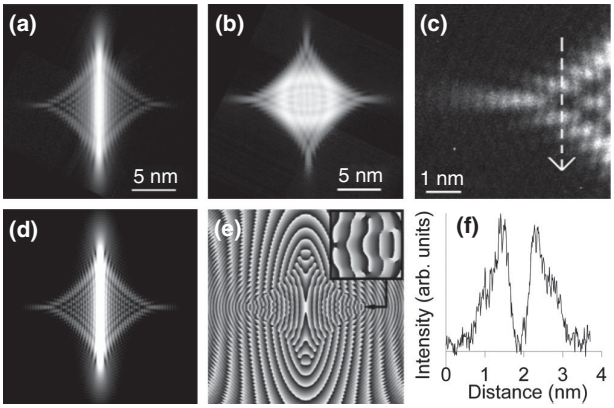

FIG. 1. (a) Experimental intensity (logarithm) near a line focus caused by condenser astigmatism. (b) Experimental intensity (logarithm) at a defocus half way between two line foci. (c) Enlarged experimental intensity for the leftmost umbilic focus in (a). (d) Logarithm of the caustic intensity computed from Eq. (1). (e) Corresponding phase computed from Eq. (1), exhibiting an array of phase vortices. (f) Five-pixel wide line plot measured from (c) showing interior intensity zeros threading vortex cores.

aperture plane describes the electron wave at a distance z along the optic axis, downstream from the aperture:

$$\Psi(x, y, z) = S(x, y, R_2)F^{-1}\{F[A(x, y)S(x, y, R_1)e^{(2\pi i/\lambda)C(x^2+3y^2)}] \times e^{-i\pi\lambda z(q_x^2+q_y^2)}\}, \quad (1)$$

where q_x and q_y are the Fourier coordinates conjugate to the Cartesian aperture-plane coordinates x and y, $\Psi(x, y, z)$ is the scalar wave function and λ is the wavelength. The symbols F and F^{-1} in Eq. (1) denote forward and inverse Fourier transforms, respectively. Primary astigmatism in the aperture plane is parametrized by the coefficient C using the polynomial form given by Kingslake [36]. The function $S(x, y, R_1)$ models the electron source as a simple spherical wave in the paraxial approximation with radius R_1, which numerically serves to condense the wave within an image array of fixed size [37]. The spherical wave $S(x, y, R_2)$ removes residual scaling of $\Psi(x, y, z)$ after propagation. Adjustment of the free parameters in Eq. (1), namely, C and R_1, produced excellent agreement between the experimental results in Fig. 1(a) and the theoretical predictions in Fig. 1(d).

The intensity logarithm and phase calculated from the diffraction integral in Eq. (1) are shown in Figs. 1(d) and 1(e), respectively. Between the umbilic foci in Fig. 1(d), spontaneously nucleated phase vortices decorate the outer edges of the caustic and some are within the interior, where intensity zeros occur in Figs. 1(a), 1(c), and 1(d). Several minima within the umbilic foci in Fig. 1(a) contain intensity zeros, which is consistent with the creation of electron vortices. However, none of the minima inside the caustic in Fig. 1(b) correspond to intensity zeros, in agreement with diffraction integral calculations. Figure 1(f) shows a five-pixel wide line plot of the intensity shown in Fig. 1(c). This

line plot confirms the presence of intensity zeros near the line focus, inside the caustic. The observation of intensity zeros is a necessary condition for the existence of vortices.

The Titan^3 80–300 TEM (FEI) provides sensitive control over lens aberrations; however, strong excitation of corrector lenses leads to parasitic aberrations and it is difficult to apply pure aberrations. To model probe cross sections accurately, it is generally necessary to characterize and account for a multitude of probe forming and imaging lens aberrations [38]; yet in Eq. (1) we have only included primary astigmatism. The detailed agreement between experiment and theory is a consequence of catastrophe theory, in that the umbilic foci represent structurally stable forms of the electron wave. To further validate this observation, astigmatism was minimized and the probe corrector was adjusted to induce primary coma, since the form of this aberration function produces the hyperbolic umbilic catastrophe [34]. Three basic examples of caustics with varying coma, collected using exposure times of 5 s per diffraction pattern are provided in the Supplemental Material [39], showing excellent agreement with earlier observations of caustics reported in coherent light optics [32,40]. To explore the coma induced diffraction catastrophe, the coma caustic was further enlarged by increasing the size of the condenser aperture to 150 μm, which diminished the contrast of the pattern. To compensate for the reduced coherence, the first condenser lens was excited to the maximum nominal setting after which the fringe contrast increased significantly. Additional coma caustics were then recorded using multiple frames (ten) and shorter exposures (3 s per frame) to offset residual beam drift.

Figure 2 compares experiment with both catastrophe theory for the hyperbolic umbilic and the diffraction integral for the coma aberration. The experimentally measured intensity in Fig. 2(c) is an average of 50 images, each exposed for 1 s and then postaligned with respect to each other. The horizontal line in Fig. 2(c) marks a single-pixel wide line plot, which is displayed in the Supplemental Material [39], showing significant fringe visibility and an array of intensity zeros. For Fig. 2(d), 10 images were acquired for 3 s, postaligned and averaged. Arrays of intensity zeros were also observed at this defocus setting, which was nominally 100 nm from that shown in Fig. 2(c). The logarithm of the intensity in Fig. 2(d) compares well to that of the hyperbolic umbilic catastrophe in Fig. 2(a) and the diffraction integral intensity logarithm in Fig. 2(e). The hyperbolic umbilic diffraction catastrophe is described by

$$\Psi(x, y, z) = \int_{-\infty}^{\infty}\int_{-\infty}^{\infty} e^{i(s_1^3+s_2^3-xs_1-ys_2-zs_1s_2)}ds_1ds_2 \quad (2)$$

where s_1 and s_2 are the relevant state variables [34] and the wave function $\Psi(x, y, z)$ is computed at focal depth z and plotted in the plane spanned by (x, y). Equation (2) was evaluated numerically with the coordinates x, y normalized by the number of pixels, to span ± 30 dimensionless units over 512×512 pixels. The integration variables s_1, s_2 were truncated to ± 3.5 and incremented in steps of 0.014

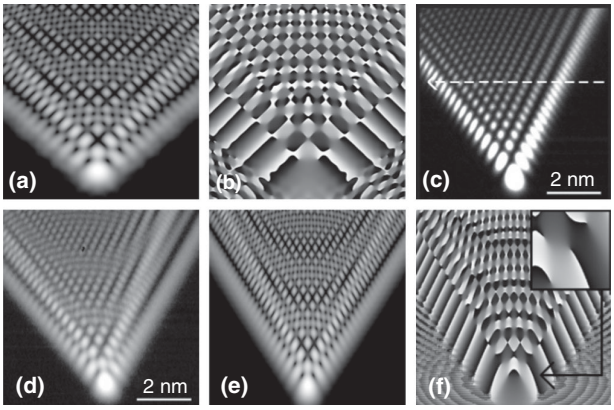

FIG. 2. (a) Logarithm of the intensity calculated using diffraction catastrophe theory. (b) Phase of the diffraction catastrophe showing a distorted lattice of vortices and antivortices. (c) Experimental intensity of coma caustic near the diffraction focus. (d) Logarithm of the experimental intensity nominally 100 nm away from the diffraction focus. (e) Logarithm of the coma caustic intensity computed from the diffraction integral in Eq. (3). (f) Phase of the coma caustic from the diffraction integral in Eq. (3).

dimensionless units. The wave function $\Psi(x, y, z)$ was then cropped to 256×256 pixels to approximately match the field of view of the experimental data. The phase of $\Psi(x, y, z)$, determined from Eq. (2), is shown in Fig. 2(b), where arrays of phase vortices decorate the interior and outer portions of the coma caustic. Similar vortices are evident in Fig. 2(f), which was computed using the diffraction integral:

$$\Psi(x, y, z) = S(x, y, R_2)F^{-1}\{F[A(x, y)S(x, y, R_1)e^{(2\pi i/\lambda)By(x^2+y^2)}] \times e^{-i\pi\lambda z(q_x^2+q_y^2)}\}, \quad (3)$$

where all symbols in Eq. (3) are identical to those in Eq. (1) except for the coefficient B, which parametrizes the degree of coma [36]. This parameter was varied until the caustic intensity pattern visually matched the experimental data.

Electron phase maps were experimentally determined from a through-focus series of images using the Gerchberg-Saxton-Misell phase retrieval algorithm [41–45] (for details, see the Supplemental Material [39]). Objective lens defocus was calibrated using power spectra of experimental images using the DIFFTOOLS suite of scripts [46]. Figure 3(a) shows the logarithm of the retrieved intensity for the first image in the through-focus series for the astigmatism caustic. Comparing Fig. 3(a) and 1(b), it is evident that most of the diffraction detail was captured by the retrieval algorithm, although the intensity minima are not as distinct. The retrieved phase map in Fig. 3(b) has a similar form to that in Fig. 1(e). Propagation of the reconstructed wave over many focal planes correctly predicted a pair of mutually orthogonal sharp line foci, as well as preservation of the caustic shape and diffraction detail with varying focus, all of which were observed in our experiments. Transverse current densities were computed

from the retrieved waves (see Supplemental Material [39]). The phase and current density vectors were rendered using software scripts based upon the algorithms of Mitchell and Schaffer [47].

Figure 3(c) shows the retrieved intensity logarithm for the first image in a through-focus series for the coma caustic. Vortices are seen to decorate the exterior of the coma caustic, with several inside the caustic shown in Fig. 3(d). Again, the intensity minima are not as distinct when compared to the experimental input. Nonetheless, the reconstructed wave reproduced much of the detail observed in the experimental images over the entire focal range. Figures 3(e) and 3(f) show the experimentally measured z component of the OAM density, determined for the retrieved wave function about a central cross section of the astigmatism caustic, displayed in SI units of 1.0×10^{-16} kg s^{-1} per electron. The root mean square value of the OAM density in Fig. 3(f) is $0.15\hbar$ nm^{-2}. The OAM density in Figs. 3(e) and 3(f) varies significantly across the beam, which is analogous to the optical interferometry measurements of Courtial *et al.* [16] for elliptical Gaussian beams. The small boxes shown in Figs. 3(e) and 3(f) have side lengths of 0.7 nm, within which the integrated OAM per electron is $42\hbar$ and $35\hbar$, respectively. Within both boxes, the corresponding average probability densities are greater than 75% of the maximum intensity over the entire field of view.

Using the reconstructed experimental wave functions, vortices were tracked throughout a propagated focal series comprising 2048^3 points and detected by measuring points of nonzero circulation in two-dimensional phase maps. Arrays of tracked vortices were represented as small spheres [48] and are shown in the Supplemental Material [39]. The vortex tracks exhibited fine detail, such as Kelvin waves along nodal lines and vortex loops. The observed nodal line instabilities were possibly due to wave perturbations from residual aberrations in the experiment, since it is known that additional plane waves can warp the structure of nodal lines in three-wave vortex lattices [49]. In accordance with known results in light optics [19], we also observed vortex loops in diffraction integral calculations, using Eqs. (1) and (3), which portrayed similar structures to nodal lines computed from the experimentally retrieved wave functions. In light optics, entire arrays of nodal loops can be formed from the superposition of four plane waves [19]. At the other extreme, tangled vortices and nodal loops can exist in self-similar speckle fields created by a ground glass screen, where the vortex lines possess a fractal structure [50]. In the context of catastrophe optics, nodal loops have been identified and studied in the hyperbolic umbilic diffraction catastrophe [51]. For our retrieved wave functions, we examined particular nodal lines in detail by cropping out all tracks except those in the subregions marked in the phase maps of Figs. 3(b) and 3(d). The electron vortex loop from the coma caustic in Fig. 4(a) shows nodal line excitations and Crow-like instabilities [52], apparently initiating dissociation into several vortex loops.

The colored plane in Fig. 4(a) shows the phase windings around adjacent sides of the loop, which highlight vortices of opposite topological charge. Figure 4(b) shows three electron vortices represented as intensity iso surfaces, which are adjacent to the umbilic focus of the astigmatism caustic shown in Fig. 3(b).

In conclusion, we have induced electron diffraction catastrophes, thereby creating distorted lattices of spontaneously nucleated electron vortices, using an aberration corrected electron microscope. We have demonstrated that phenomena, such as Crow-type nodal-line instabilities and nonlinear effects, such as pair creation or annihilation, can be measured for matter waves that obey a linear wave equation. Our singular electron optics observations closely

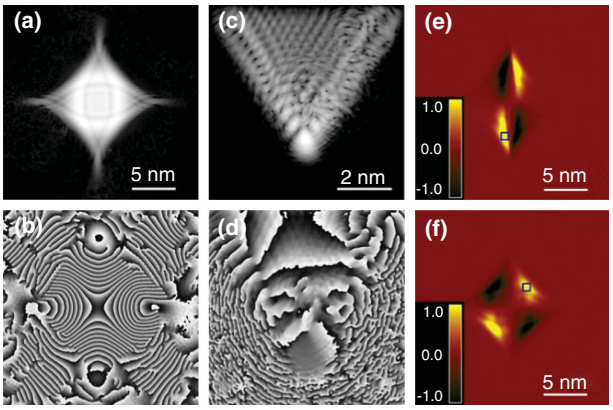

FIG. 3 (color). (a) Logarithm of the reconstructed intensity for the first image in the through focus series of astigmatic images. (b) Corresponding retrieved phase with vortices surrounding the caustic. (c) Logarithm of the reconstructed intensity for the first image in the through focus series of five coma images. (d) Corresponding retrieved phase. (e) The z component of the orbital angular momentum density for the retrieved astigmatism caustic wave function near one line focus, and (f) a defocus between the two line foci.

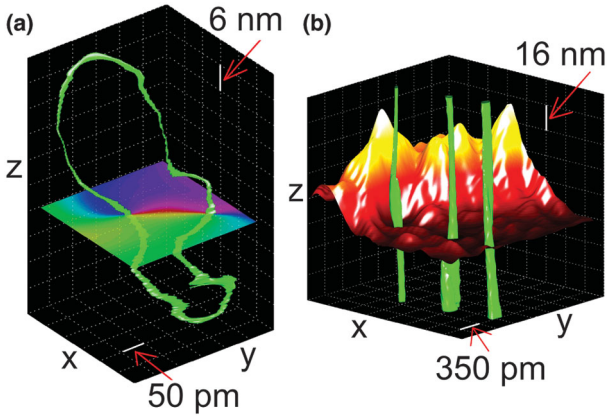

FIG. 4 (color). (a) Electron vortex loop observed in the interior of the coma caustic in Fig. 3, where the color-coded phase map shows a vortex-antivortex pair, which nucleates and annihilates at specific points along the optic z axis. (b) Vortex lines puncturing the image plane for the astigmatism caustic of Fig. 3(b); the color-coded part represents the intensity.

parallel experimental and theoretical findings in light optics and thereby raise the possibility of creating topologically knotted electron waves [53]. Using experimentally retrieved electron wave functions, we have also mapped the OAM density per electron for astigmatic wave fields.

T. C. P. thanks the Monash University electron scattering group for useful comments. The authors acknowledge use of facilities within the Monash Centre for Electron Microscopy. This research used equipment funded by the Australian Research Council Grant No. LE0454166. Funding from the Australian Research Council Discovery Project Grant No. DP1092745 is also gratefully acknowledged.

*Corresponding author.
timothy.petersen@monash.edu

[1] L. J. Allen, H. M. L. Faulkner, K. A. Nugent, M. P. Oxley, and D. Paganin, Phys. Rev. E **63**, 037602 (2001).
[2] L. J. Allen, H. M. L. Faulkner, M. P. Oxley, and D. Paganin, Ultramicroscopy **88**, 85 (2001).
[3] M. Uchida and A. Tonomura, Nature (London) **464**, 737 (2010).
[4] J. Masajada and B. Dubik, Opt. Commun. **198**, 21 (2001).
[5] V. Ravikumar, R. P. Rodrigues, and V. P. Dravid, J. Am. Ceram. Soc. **80**, 1117 (1997).
[6] K. W. Nicholls and J. F. Nye, J. Phys. A **20**, 4673 (1987).
[7] R. Vincent, W. J. Vine, P. A. Midgley, P. Spellward, and J. W. Steeds, Ultramicroscopy **50**, 365 (1993).
[8] M. Terauchi, K. Tsuda, O. Kamimura, M. Tanaka, T. Kaneyama, and T. Honda, Ultramicroscopy **54**, 268 (1994).
[9] A. F. Moodie, J. Etheridge, and C. J. Humphreys, Acta Crystallogr. Sect. A **52**, 596 (1996).
[10] P. N. H. Nakashima, A. F. Moodie, and J. Etheridge, Acta Crystallogr. Sect. A **63**, 387 (2007).
[11] J. Verbeeck, H. Tian, and P. Schattschneider, Nature (London) **467**, 301 (2010).
[12] B. J. McMorran, A. Agrawal, I. M. Anderson, A. A. Herzing, H. J. Lezec, J. J. McClelland, and J. Unguris, Science **331**, 192 (2011).
[13] J. Verbeeck, H. Tian, and A. Beche, Ultramicroscopy **113**, 83 (2012).
[14] J. Verbeeck, P. Schattschneider, S. Lazar, M. Stoger-Pollach, S. Loffler, A. Steiger-Thirsfeld, and G. Van Tendeloo, Appl. Phys. Lett. **99**, 203109 (2011).
[15] M. V. Berry, J. Opt. A **11**, 094001 (2009).
[16] J. Courtial, K. Dholakia, L. Allen, and M. J. Padgett, Opt. Commun. **144**, 210 (1997).
[17] M. V. Berry, J. F. Nye, and F. J. Wright, Phil. Trans. R. Soc. A **291**, 453 (1979).
[18] M. S. Soskin and M. V. Vasnetsov, in *Progress in Optics*, edited by E. Wolf (Elsevier, Amsterdam, 2001), p. 219.
[19] M. R. Dennis, K. O'Holleran, and M. J. Padgett, in *Progress in Optics*, edited by E. Wolf (Elsevier, Amsterdam, 2009), p. 293.
[20] A. G. Peele, K. A. Nugent, A. P. Mancuso, D. Paterson, I. McNulty, and J. P. Hayes, J. Opt. Soc. Am. A **21**, 1575 (2004).
[21] G. W. Farnell, Can. J. Phys. **36**, 935 (1958).
[22] B. T. Hefner and P. L. Marston, J. Acoust. Soc. Am. **106**, 3313 (1999).
[23] M. V. Berry, Adv. Phys. **25**, 1 (1976).
[24] J. F. Nye, *Natural Focusing and Fine Structure of Light: Caustics and Wave Dislocations* (Institute of Physics Publishing, Bristol, 1999).
[25] A. Boivin, J. Dow, and E. Wolf, J. Opt. Soc. Am. **57**, 1171 (1967).
[26] K. M. Pavlov *et al.*, Phys. Rev. A **83**, 013813 (2011).
[27] G. Ruben and D. M. Paganin, Phys. Rev. E **75**, 066613 (2007).
[28] D. R. Scherer, C. N. Weiler, T. W. Neely, and B. P. Anderson, Phys. Rev. Lett. **98**, 110402 (2007).
[29] G. Ruben, D. M. Paganin, and M. J. Morgan, Phys. Rev. A **78**, 013631 (2008).
[30] B. R. A. Nijboer, Physica (Amsterdam) **13**, 605 (1947).
[31] K. Nienhuis and B. R. A. Nijboer, Physica (Amsterdam) **14**, 590 (1949).
[32] E. Wolf, Rep. Prog. Phys. **14**, 95 (1951).
[33] P. W. Hawkes and E. Kasper, *Principles of Electron Optics* (Academic Press, London, 1996), Vol. 3.
[34] M. V. Berry and C. Upstill, in *Progress in Optics*, edited by E. Wolf (Elsevier, New York, 1980), p. 257.
[35] M. Born and E. Wolf, *Principles of Optics* (Cambridge University Press, Cambridge, England, 1999), Seventh (Expanded) Edition.
[36] R. Kingslake, Trans. Opt. Soc. **27**, 94 (1925).
[37] D. M. Paganin, *Coherent X-ray Optics* (Oxford University Press, New York, 2006).
[38] C. Dwyer, S. Lazar, L. Y. Chang, and J. Etheridge, Acta Crystallogr. Sect. A **68**, 196 (2012).
[39] See the Supplemental Material at http://link.aps.org/supplemental/10.1103/PhysRevLett.110.033901 for examples of three measured coma caustics, coma intensity zeros, explicit details of phase retrieval parameters, retrieved electron vortices and transverse current densities, and plots of vortex tracks in experimentally retrieved wave functions.
[40] R. Kingslake, Proc. Phys. Soc. London **61**, 147 (1948).
[41] R. W. Gerchberg and W. O. Saxton, Optik (Stuttgart) **35**, 237 (1972).
[42] D. L. Misell, J. Phys. D **6**, 2217 (1973).
[43] L. J. Allen and M. P. Oxley, Opt. Commun. **199**, 65 (2001).
[44] L. J. Allen, W. McBride, N. L. O'Leary, and M. P. Oxley, Ultramicroscopy **100**, 91 (2004).
[45] C. T. Koch, Ultramicroscopy **108**, 141 (2008).
[46] D. R. G. Mitchell, Microsc. Res. Tech. **71**, 588 (2008).
[47] D. R. G. Mitchell and B. Schaffer, Ultramicroscopy **103**, 319 (2005).
[48] R. A. Sayle and E. J. Milnerwhite, Trends Biochem. Sci. **20**, 374 (1995).
[49] K. O'Holleran, M. J. Padgett, and M. R. Dennis, Opt. Express **14**, 3039 (2006).
[50] K. O'Holleran, M. R. Dennis, F. Flossmann, and M. J. Padgett, Phys. Rev. Lett. **100**, 053902 (2008).
[51] J. F. Nye, J. Opt. A **8**, 304 (2006).
[52] S. Crow, AIAA J. **8**, 2172 (1970).
[53] M. R. Dennis, R. P. King, B. Jack, K. O'Holleran, and M. J. Padgett, Nat. Phys. **6**, 118 (2010).